Core-antiresonance-based terahertz cavities and applications [Invited]

Yongpeng Han (韩永鹏)[1], Yangjun Mei (梅养军)[1], Chang Liu (刘昶)[2], Li Lao (劳力)[3], Yao Yao (姚瑶)[1], Jiahao Xiao (肖家豪)[1], Jiayu Zhao (赵佳宇)[1*], and Yan Peng (彭滟)[1,4]

[1] Terahertz Technology Innovation Research Institute, Terahertz Spectrum and Imaging Technology Cooperative Innovation Center, Shanghai Key Laboratory of Modern Optical System, University of Shanghai for Science and Technology, Shanghai 200093, China
[2] Shanghai Institute of Optics and Fine Mechanics, Chinese Academy of Sciences, Shanghai 201800, China
[3] Tera Aurora Electro-optics Technology Co., Ltd., Shanghai 200093, China
[4] Shanghai Institute of Intelligent Science and Technology, Tongji University, Shanghai 200092, China

This work presents a brief review of our recent research on an antiresonant mechanism named core antiresonant reflection (CARR), which leads to a broadband terahertz (THz) spectrum output with periodic dips at resonant frequencies after its transmission along a hollow-core tubular structure (e.g., a paper tube). The CARR theory relies only on parameters of the tube core (e.g., the inner diameter) rather than the cladding, thus being distinct from existing principles such as the traditional antiresonant reflection inside optical waveguides (ARROWs). We demonstrate that diverse tubular structures, including cylindrical, polyhedral, spiral, meshy, and notched hollow tubes with either transparent or opaque cladding materials, as well as a thick-walled hole, could indeed become CARR-type resonators. Based on this CARR effect, we also perform various applications, such as pressure sensing with paper-folded THz cavities, force/magnetism-driven chiral polarization modulations, and single-pulse measurements of the angular dispersion of THz beams. In future studies, the proposed CARR method promises to support breakthroughs in multiple fields by means of being extended to more kinds of tubular entities for enhancing their interactions with light waves in an antiresonance manner.

Keywords: antiresonance; core; cladding; tubular structure; application.
DOI: 10.3788/COL202321.110005

1. Introduction

The antiresonance effect facilitates numerous remarkable applications in the fields of physics, biophotonics, and material science, including the utilization of low-loss waveguides, which span from the ultraviolet[1–4] to the terahertz (THz)[5] bands, as well as the development of optofluidic chips for gas/liquid atomic spectroscopy[6–10]. Moreover, it enables the creation of multifunctional sensors for various scenarios, such as biochemical sample analysis[11,12] and measurements of physical properties[13,14] like displacement, strain, pressure, and temperature.

In this work, we provide an overview of our recent investigations into a new antiresonant phenomenon termed core antiresonant reflection (Core-ARR or CARR)[15–17], which yields a broadband THz spectrum with periodic dips at resonant frequencies when THz waves traverse a hollow core tubular structure, such as a single-layer paper tube. Unlike existing principles, e.g., the traditional antiresonant reflection inside hollow optical waveguides (ARROWs)[1–5], our CARR theory relies

solely on characteristics of the tube core (e.g., the inner diameter) instead of the cladding thickness or refractive index, making it fundamentally distinct from established approaches. More importantly, the CARR mechanism enables more kinds of tubular structures to resonate with light waves, thus enhancing the light–matter interactions in corresponding fields, where tubular entities are frequently studied[1–10,18–38]. Therefore, exciting opportunities are offered by the proposed CARR method for advancements in both fundamental understanding and practical applications.

The organization of this article is as follows. In Section 2, we derive the concept of CARR from the classical Fabry–Perot (F–P) cavity principle, highlighting its connection to traditional antiresonance[1–5] and multimode interference theories[26,27] while also examining its distinct characteristics. In Section 3, we demonstrate that diverse tubular structures, such as cylindrical, polyhedral, spiral, meshy, and notched hollow tubes with either transparent or opaque cladding materials, as well as a thick-walled hole, could indeed become CARR-type resonators.

In Section 4, we perform applications based on the CARR effect, including the pressure sensing with paper-folded THz cavities, force/magnetism-driven chiral polarization modulations, and single-pulse measurements of the angular dispersion of THz beams. In Section 5, we briefly introduce the numerical simulation method of the CARR effect. Finally, in Section 6, we summarize the whole work and put forward future prospects.

2. Origin of the CARR Mechanism

2.1. From the F–P cavity to the CARR cavity

Here, we show the deduction from the traditional F–P cavity to our CARR effect. It is well known that an F–P cavity consists of two parallel surfaces, as shown in Fig. 1(a-I). In a condition of a broadband light incidence, only optical waves in resonance with the cavity can be transmitted. The transmission spectrum is a series of resonance peaks at frequencies of f_m ($m = 1, 2, 3 \ldots$), which can be calculated by the F–P formula,

$$f_m = \frac{mc}{2nD \cos \theta},$$ (1)

and relevant parameters are described in Fig. 1(a-II), where c is the speed of light in vacuum, n is the refractive index between two reflecting interfaces with separation of D, and θ is the incident angle of light on the interface.

By contrast, unfortunately, the nonresonantly spectral components are strongly attenuated during phase-mismatching oscillations inside the cavity [marked with a red cross in Fig. 1(a-I)]. However, this wasted optical energy also carries the complete information of resonance frequencies (as spectral dips, instead). One way to save the nonresonance wave, intuitively, can be increasing its reflectivity on both plates by enlarging θ, and then guiding it out of the cavity in a direction parallel to the plates, as shown in Fig. 1(a-III). This time, the light source needs to be set on the top of the cavity. Moreover, the parallel plates should be bent into two half-cylinders or even rolled into a whole cylindrical tube [Fig. 1(b)] in order to fit the incident divergent light beam and avoid side leakages of the guided energy. Finally, the antiresonant components could be harvested from the tube exit; this process is schematically drawn in Fig. 1(c-I).

Based on the above analyses, it appears that the term "leaky F–P cavity" would be appropriate for our proposed scheme. Additionally, the F–P equation [i.e., Eq. (1)] indeed offers a sound explanation for the observed phenomena in our studies[15–17]. However, in the end, we decided to name our scheme the core antiresonant reflection (core-ARR or CARR), drawing parallels to traditional antiresonance (also known as ARROW),
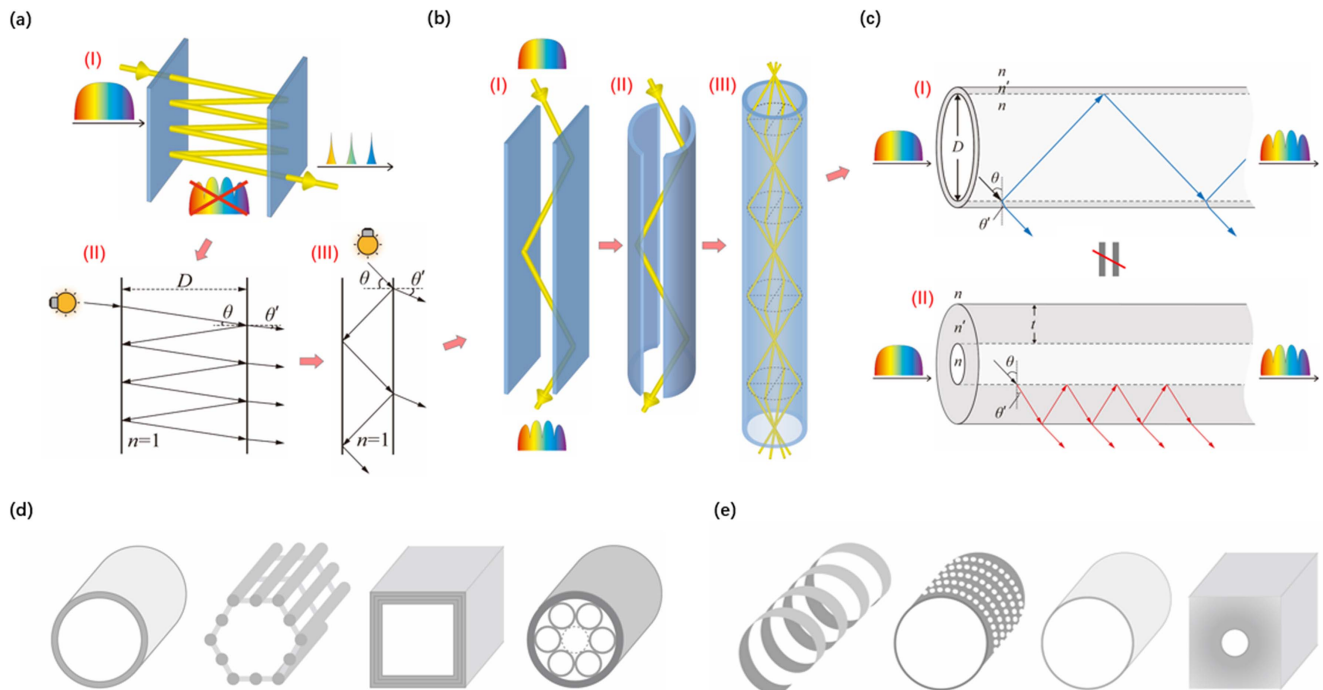

Fig. 1. Origin of the CARR principle. (a) (I) F–P cavity and (II) relevant parameters; (III) the light source is set on the top of the F–P cavity for glancing incidence, and the antiresonant frequency components are guided out from the bottom of the cavity. (b) To accommodate the incident light beam from a point source on the tube axis, the parallel plates of the F–P cavity are bent into a fully enclosed cylindrical wall. (c) The main distinction between the proposed CARR theory and traditional antiresonance lies in the location of optical oscillations, occurring either (I) in the central core or (II) in the cladding. (d) Several representative ARROWs, including a cylindrical pipe[5], a hexagonal cage[6,7], a quadrilateral multilayer channel[8–10], and a ring-nested fiber[1]. (e) Several representative tubular geometries wherein the proposed CARR effect is applicable rather than the traditional antiresonance, including a helix[18,19], a multihole tube[20–22], an ultrathin tube[23,24], and a thick-wall hole[25]. (d), (e) Adapted from Ref. [15] under the license CC BY 4.0.

due to the similarities between these two mechanisms, as discussed below.

2.2. Comparison between CARR and traditional antiresonance effects

The antiresonance in the literature is a crucial interaction between light and tubular structures[1–5] that occurs during light waves oscillation inside the F–P-like cladding of hollow tubes, as illustrated in Fig. 1(c-II). Consequently, resonant components penetrate the cladding (leaking out), while the antiresonant ones are guided along the central core, thereby creating a broadband transmission mode with periodical spectral dips (corresponding to resonant frequencies). Currently, fundamental connections have been built between the traditional antiresonance effect and the waveguide's cladding, whose structural morphology might be either simple or complex, as displayed in Fig. 1(d), but necessarily acting as a quasi-F–P cavity. In view of this F–P dependence, our CARR method shares similarities with the conventional ARROW. Both of them can be regarded as leaky F–P-like cavities, inside which reflections need to be smaller than 100% for each bounce, and the output spectra have periodic dips. The primary distinction between our CARR and ARROW lies in the area of wave oscillations, as depicted in Fig. 1(c), in the core and cladding, respectively. It is for this reason that we named our proposal the core antiresonant reflection (core-ARR, or CARR for short).

Furthermore, the F–P cladding condition of typical antiresonance poses limitations on many other tubular structures [Fig. 1(e)], preventing them from interacting with lights in an antiresonance fashion. For example, for the helical materials, such as chiral ceramics[18] and elastic metal springs[19], their spiral walls obviously cannot function as equivalent F–P units. The same applies to a multihole tube with mesh-structured cladding[20–22]. Additionally, in the case of the self-rolled-up 2D material[23,24], the cladding is usually too thin to support internal oscillations and resonances of light waves. This time, our CARR method could equip the tubes in Fig. 1(e) with its antiresonant capability, owing to the fact that the CARR theory focused on the commonality of hollow cores in these tubular structures. These cores inherently form curved leaky F–P cavities, which theoretically permit antiresonances, as depicted in Fig. 1(c-I). This unique feature is less dependent on the cladding's materials and construction, thus expanding the antiresonance effect to a broader range of tubular materials, including those shown in Fig. 1(e), and providing them with a new perspective on strengthening interactions with light. Example application experiments are carried out in Sections 3 and 4.

2.3. Comparison between CARR and the multimode interference effects

Apart from the typical antiresonance, the CARR effect is also similar to, but different from, the multimode interference observed in hollow core THz waveguides[26,27]. As for the latter, briefly, multiple modes are characterized by different effective propagation velocities (i.e., phase differences) along the waveguide, and the modal interference results in the periodically-distributed maxima and minima in the output spectrum. This interference behavior is normally confined inside the waveguide core, without the requirement for light to leak out. For example, a metallic tube was employed for the multimode interference of THz waves[26], which were blocked from transmitting through the metal cladding.

However, this property is obviously against the condition for the CARR theory, where both the transmission and reflection of THz waves by the tube wall are necessary as a fundamental quasi-F–P effect, as shown in Figs. 1(a)–1(c). This can also be seen in Section 3, where the spectral dip phenomenon was not observed with a metallic tube in our case, whereas under similar conditions, a meshy metallic tube exhibited dips in the spectrum. In other words, the transmissivity is one of the essential conditions for using a CARR-type cavity or waveguide, and the interference outside the tube wall is more crucial than that inside the tube core, which results from the leaky F–P effect. Therefore, the CARR effect and multimode interference are two distinct mechanisms.

3. Experimental Verification of the CARR Theory

3.1. Experimental configurations

As shown in Fig. 2(a), common A4 paper can be used to produce CARR tubes. Specifically, a piece of plain A4 paper was wet by water and tightly coated on a cylindrical mold. Alternatively, one may drip liquid glue on the overlap area, rather than totally wetting the paper. The mold would not be removed until the paper dried. In comparison, the second means in Fig. 2(a) is similar, except for its winding fashion of a paper tape on the cylindrical mold. A paper helix can also be made following the winding fashion but using narrower paper tapes to create helical pitches. All CARR tubes in Fig. 3 were made in similar ways, and the inner diameter (D), cladding thickness (t), and length (L) were easily handmade into around 10 mm, 0.1–2 mm (0.1 mm for the paper thickness), and 15 cm.

Then, CARR tube cavities were tested in our all-fiber THz-TDS (time-domain spectroscopy) setup, as shown in Fig. 2(b). Briefly, a fiber laser device delivered femtosecond laser pulses in two paths as pump and probe, respectively, which then excited the THz transmitter/detection module. Each module was a group of a photoconductive antenna (PCA) emitter/receiver and two THz converging lenses (TPX). To ensure the accuracy of these optical devices, we employed a cage system (Thorlabs) to maintain their alignment, as shown in Fig. 2(c). Between the two modules, a rail and linkage system was also adopted to ensure collimation. Furthermore, there are front and rear apertures and two holders, enabling the cylindrical tube cavity's repositioning accuracy.

3.2. Observation of the CARR phenomena with different cladding materials

Based on the CARR technique, one has a wide range of choices of materials and structures of the tube cladding. Aiming at
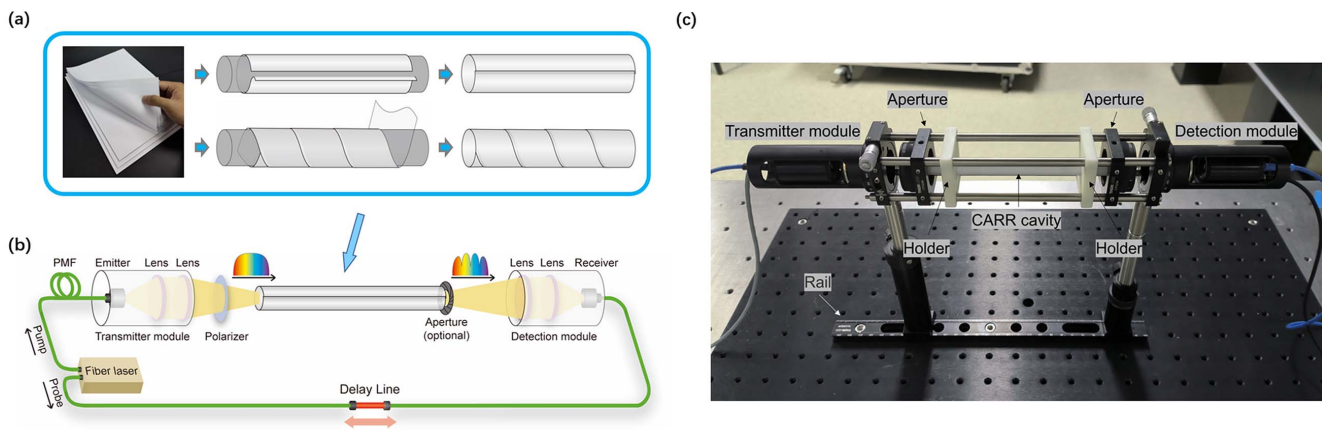
Fig. 2. (a) Two examples to make cylindrical tubes by paper; (b) the CARR tube was tested in a typical THz-TDS setup. (c) The cage system for positioning the CARR cavity between the THz transmitter and receiver. (a), (b) Adapted from Ref. [15] under the license CC BY 4.0.

verifying this point, we tested various tubular entities, as shown in Fig. 3, revealing the versatility of the CARR theory.

In Fig. 3(a), nonpolar materials with low material loss in the THz band were rolled into single-layer tubes, including the A4 paper, the coated paper from magazines, the sandpaper, and the PVC plastic. Beside each tube picture, the output THz spectra are presented with a vertical offset for clarity, whose resonant frequencies are highlighted by gray dashed lines. Furthermore, as shown at the bottom, a paper helix was also made. Surprisingly, the resultant THz spectrum matches well with the aforementioned ones.

By contrast, for a tube made of polar materials in the THz band (e.g., metal film), its cladding is opaque for THz waves, contradicting the CARR condition [Fig. 1(c-I)]. Hence, the CARR effect (periodic spectral dips) cannot be observed in the top signal of Fig. 3(b). However, the absence of this CARR

nature can be easily rectified by enhancing the light transmission through the tube cladding, such as by using a longitudinal slot, porous/multihole structures, or helical air clearances added to the cladding wall. As indicated in Fig. 3(b), from the second signal to the last one, all these spectral signals were restored with periodic dips (i.e., resonant frequencies).

Till now, both dielectric and metal materials have achieved an unprecedented access to antiresonantly interact with light modes. Moreover, the tube appearances in Fig. 3 are frequently found on both natural and artificial tubular structures, such as cylindrical[5,20,21,28,29], polyhedral[6–10,30,31], and helical ones[18,19,32–34]. Thus, the proposed CARR method might pave the way toward interdisciplinary applications in various fields, e.g., based on spiral materials like chiral inorganic materials[18], metal springs[19], carbon coils[35], and helical proteins/DNA[36–38].
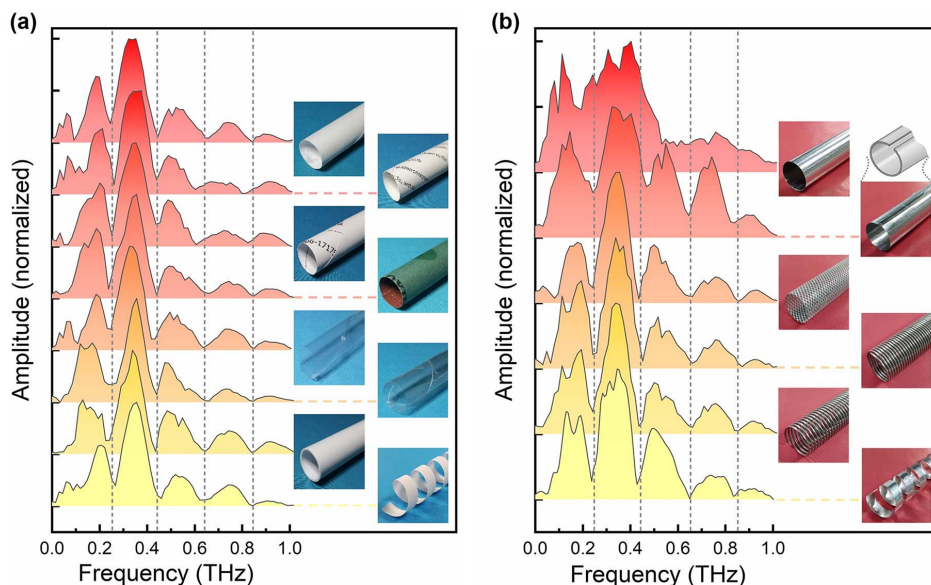

Fig. 3. Diversity of the CARR cladding materials. (a) Normalized transmission spectra (left) through tubes (right) made of different nonpolar materials with high transparency in the THz band; (b) similar spectra with (a) except for the cladding made by polar materials instead. Note that, the single-layer tinfoil tube on top is not a CARR cavity, and thus is without dips in its spectrum. (a), (b) Adapted from Ref. [15] under the license CC BY 4.0.
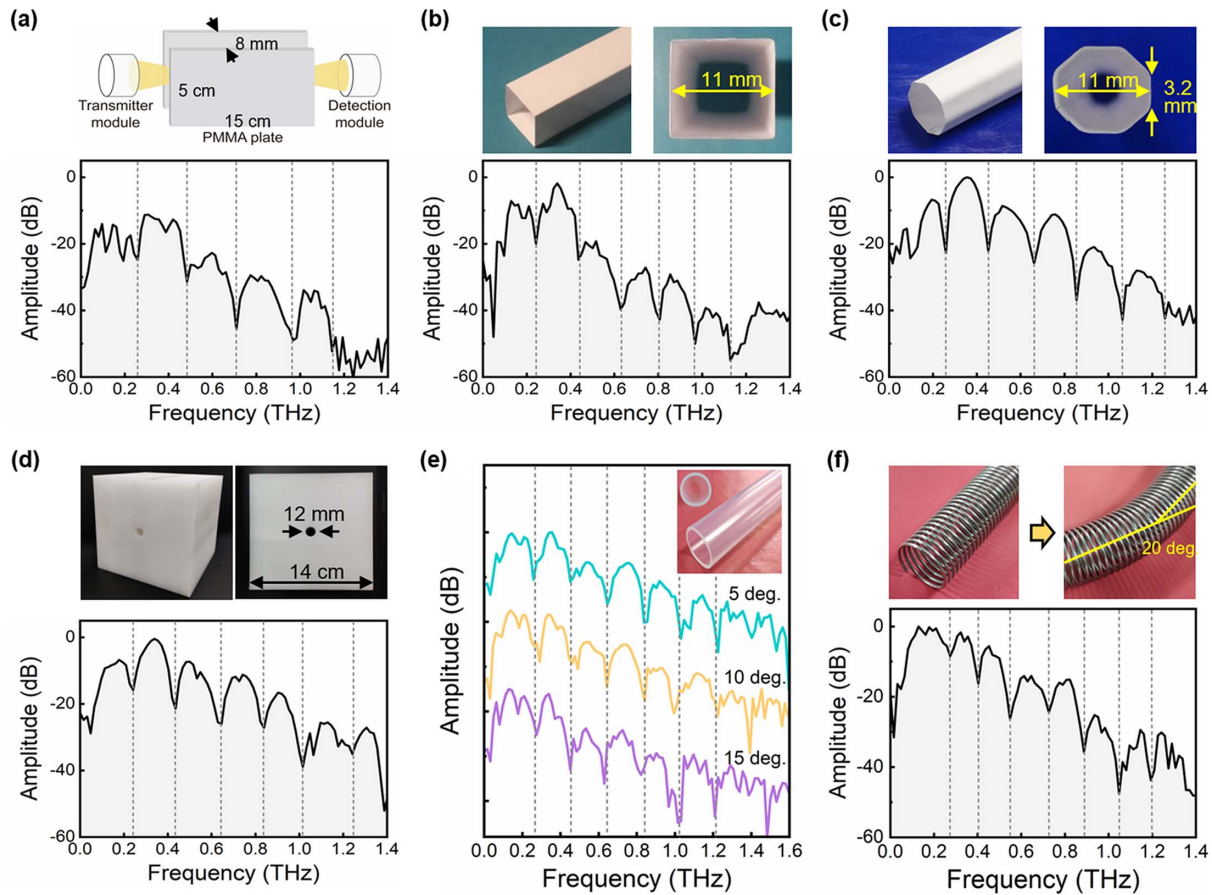
Fig. 4. (a) Parallel plates, (b) quadrilateral and (c) octagonal paper tubes, (d) hollow air hole with large wall thickness, (e) bent plastic tube, and (f) metallic spring with corresponding CARR spectra. (a)–(d) Adapted from Ref. [15] under the license CC BY 4.0.

It is also worth mentioning that, for tubes with cladding thickness several times larger than the THz wavelength, like the PVC tubes in Fig. 3(a), the coexistence of traditional antiresonances and CARR can be observed[15]. However, the CARR effect can only dominate in short tubes and will be completely converted into traditional antiresonant modes in long waveguides[15]. Moreover, the measured loss of the CARR spectrum is larger than $0.036\ \mathrm{cm}^{-1}$. Therefore, the CARR effect is not suitable for long-distance THz transmission, but is better applied inside short tubular structures for making functional devices like the three application examples in Section 4.

3.3. Observation of the CARR phenomena with different cladding morphologies

Besides the wide range of available cladding materials proved above, another impressive characteristic of CARR resonators is the flexibility of their cladding construction.

As shown in Figs. 4(a)–4(c), a pair of parallel plates made of polymethyl methacrylate (PMMA) and polyhedral tubes made by paper folding with quadrangular and octagonal cross sections were tested, respectively. Accordingly, the transmission spectra are shown in the lower part of Figs. 4(a)–4(c), where the vertical

dashed lines highlight the resonant frequencies caused by the CARR effect. In Fig. 4(d), a 12-mm-diameter air hole centered inside bulk polyethylene (PE) with a length of 15 cm was experimented with, and the resultant THz spectrum also featured the CARR behavior. Moreover, slight bending of CARR structures would not break the antiresonance results, as shown in Figs. 4(e) and 4(f). All these evidences strongly revealed the structural diversity of tubular cavities offered by the suggested CARR mechanism.

4. Applications Based on CARR Cavities

In order to investigate the proposed CARR nature, comprehensive experiments were carried out in the previous section by adopting diverse tubular materials and structures to detect the CARR spectra. In this section, several representative applications have been performed based on these CARR-type resonators.

4.1. Pressure sensing via paper-folded CARR cavities

Due to the ability of making a single sheet of paper into a THz resonant cavity (Figs. 3 and 4), which inherits the foldable characteristic of paper, it is natural for one to come up with an idea of combining the paper folding and the deformation of the paper
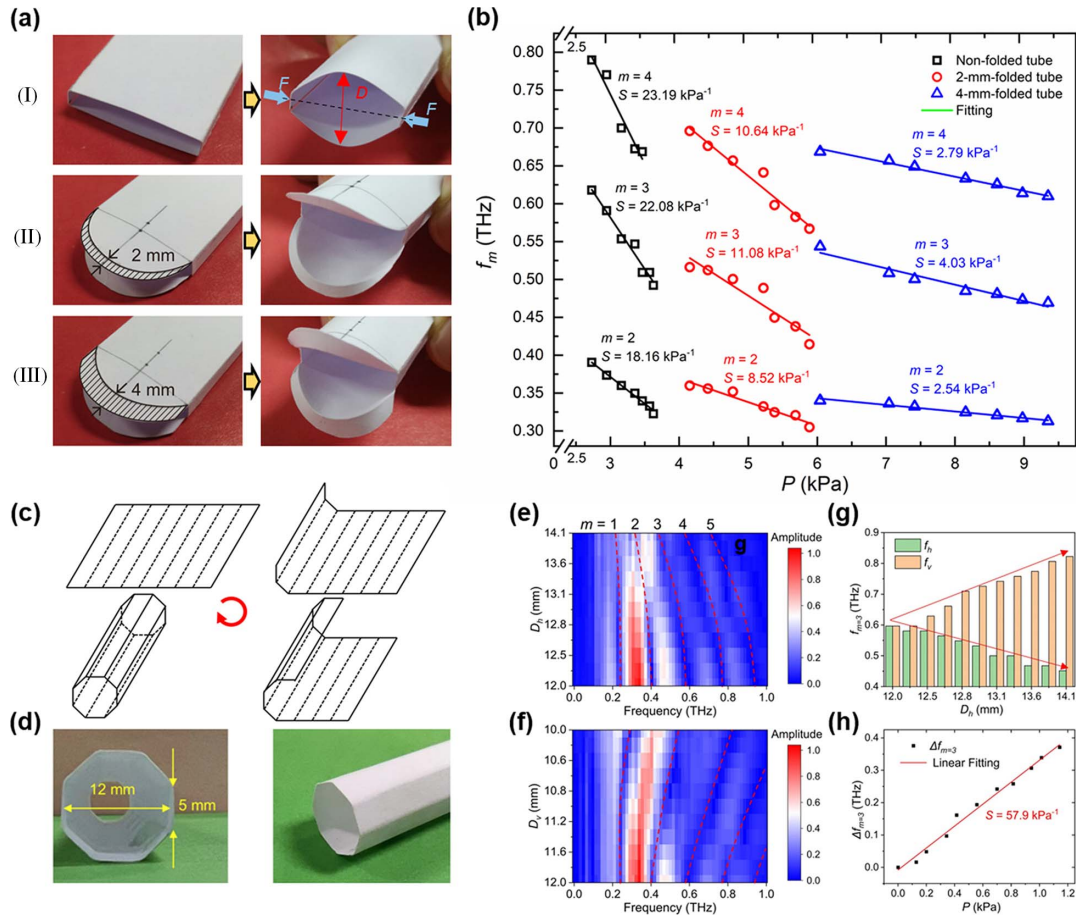
Fig. 5. CARR-type applications on sensing the ambient stress by considering single or orthogonal polarization directions. (a) The CARR tubes used with different sensitivities S and pressure P ranges due to different structures (without/with folded-up ends) of the tube claddings; (b) correlations between resonant frequencies f_m and the applied P for the above tubes; (c), (d) folding process of an octagonal paper tube and its photos; (e), (f) THz spectra of orthogonally polarized components during the pressure-sensing process; (g) corresponding evolution of resonant frequencies (f_h and f_v) at $m = 3$; (h) distribution of $\Delta f_{m=3}$ with respect to the applied pressure P. (a), (b) Adapted from Ref. [15] under the license CC BY 4.0; (c)–(h) adapted with permission from Ref. [16], © The Optical Society.

cavity length. In this way, when the shape of the paper cavity is altered by ambient factors, the cavity length and resonance frequency locations are also changed. As a result, the spectral sensing functionality can be achieved by the paper-folded CARR cavity. The advantage of this approach is that by using different types of origami, the structure of the cavity and the manner in which the cavity length varies can be customized to meet the requirements of different application scenarios[16].

Taking pressure sensing as an example, as shown in Fig. 5(a-I), we fabricated a quadrilateral paper tube. The transmitted THz spectra and the corresponding pressure values were recorded while we incrementally varied the separation distance D (red double-headed arrow) between two long sides. Three resonant frequencies f_m ($m = 2, 3,$ and 4) are extracted and plotted as functions of P in Fig. 5(b) as black open squares, accompanied by linear fittings. At present, the bearable P region around 3 kPa with a sensitivity of 23 kPa^{-1} has been successfully achieved. Here, the sensing sensitivity is evaluated by $S = |\delta(\Delta f / f_0)/\delta P|$, where f_0 is the resonance frequency without external loads, and Δf is the variation of f_0 under a certain pressure P. Next, we introduced

a modification to this rectangular tube by adding two round edges to both ends, which were then folded up, as demonstrated in Fig. 5(a-II, III). This origami-based procedure conveniently altered the cladding properties[24]. With the existence of folded edges, the cladding structure was reinforced, as right now the same change of the separation D required larger external pressure to counteract the heavier edge bending. Consequently, the spectral response regions of the two edge-folded CARR tubes differed from that of the rectangular one, as shown in Fig. 5(b), spanning 4–6 kPa and 6–9.5 kPa, respectively. Simultaneously, all S values remained at a high level of >2 kPa^{-1}.

Regarding the pressure sensing applied above, only the D variation in one single polarization direction was considered. By contrast, next, we focused on the octagonal tube for two specific reasons. (i) It can be flexibly folded and deformed under external forces, which could be more practicable than other tubes. Similar structures with less or more sides, e.g., a quadrilateral or dodecagonal tube, would suffer from either the lack of origami flexibility, or the small plate area for optical beam reflections. And (ii), it has four pairs of F–P-like parallel plates,

which allows simultaneous tuning of two F–P cavities in orthogonal directions with only one press on top of the cavity, benefiting from the origami-induced deformation. Hence, the corresponding sensitivity of the octagonal cavity is expected to be larger than the quadrilateral tubes used.

The designed octagonal structure is shown in Figs. 5(c) and 5(d), which was forced on the top, and its D_h (or D_v) increased (or decreased) away from their initial values (12 mm). The monitored THz spectra are shown in Figs. 5(e) and 5(f) for the orthogonal polarizations, respectively. It can be clearly seen that resonant frequencies f_h (or f_v) at different m induced by D_h (or D_v) decreased (or increased) as expected, which are highlighted by red dashed lines. This phenomenon is further quantified in Fig. 5(g) at $m = 3$, based on which $\Delta f_{m=3} = |f^h_{m=3} - f^v_{m=3}|$ is calculated and presented in Fig. 5(h) as black squares. By linearly fitting the relationship between $\Delta f_{m=3}$ and the pressure P as the red line, the calculated S is 57.9 kPa^{-1} in the range of 0–1.14 kPa. This value achieved by cross-polarization tuning is more than twice as large as the 23.19 kPa^{-1} previously obtained with the quadrilateral paper cavity, which merely considered f_m variations in a single polarization direction.

Compared with recent publications[39–46], our sensitivity is also competitive[16]. For example, a pressure sensor[39], fabricated by sandwiching porous MXene-impregnated tissue paper between a biodegradable polylactic acid (PLA) thin sheet and an interdigitated electrode-coated PLA thin sheet, has a maximum pressure sensitivity of 3.81 kPa^{-1}, which is much lower than our value.

4.2. Force/magnetism-driven THz polarization modulations based on CARR cavities

In the aforementioned pressure-sensing process, orthogonal CARR cavity lengths were adjusted. Simultaneously, the relative time differences of the orthogonal THz polarization components were also changed, which would result in a conversion of the output THz polarization state. Following this clue, we continued operation on the above octagonal setup and applied the stress only at the exit of the tubular cavity, as shown in Fig. 6(a). Then the inner diameters of D_h and D_v were varied slightly around the rear of the tube, which would not significantly affect the CARR effect, but would change the optical path and the
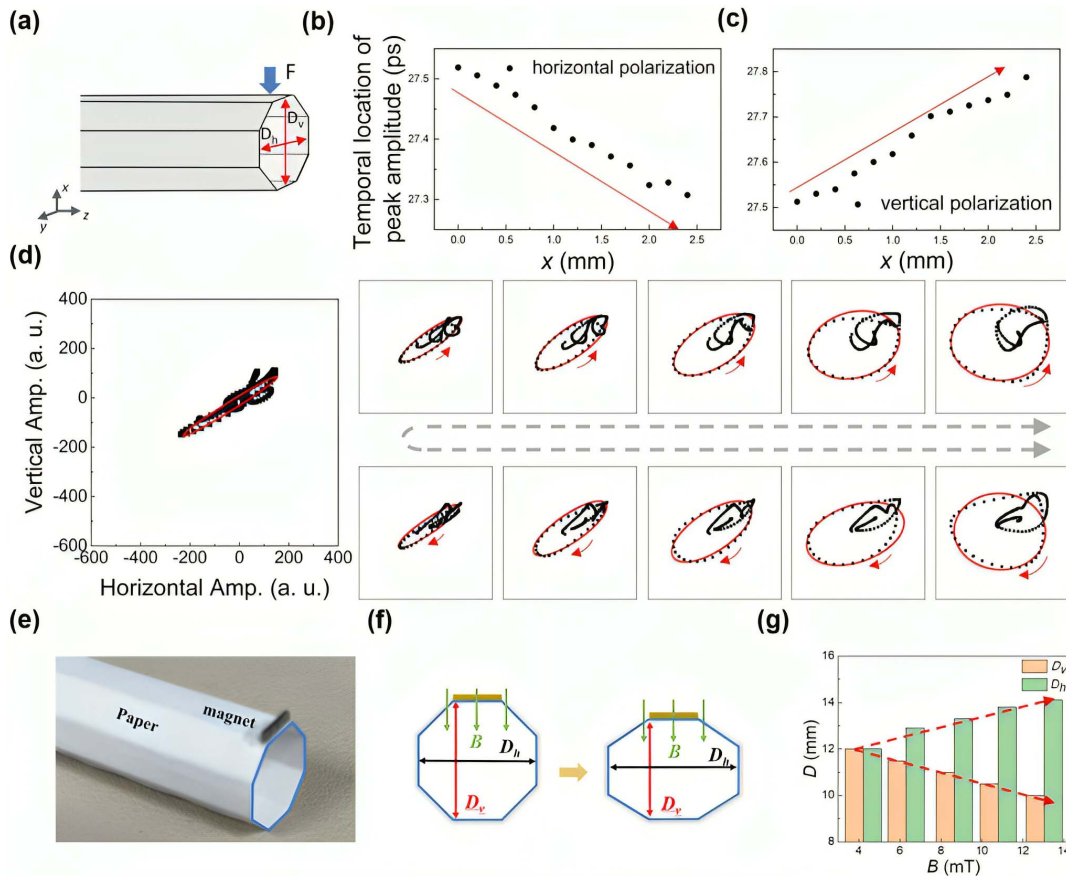

Fig. 6. THz polarization modulations by the octagonal paper cavity. (a) Schematic of the external force applied on the rear of the cavity; (b), (c) time variation of the THz waveform peak retrieved from the orthogonal polarization components; (d) evolution of linear-elliptical-circular polarization states of the output cavity mode; (e) magnetism-driven scheme of THz polarization modulation by attaching a magnet at the tube port, which is then exposed to the external magnetic field; (f), (g) deformation of the tube's cross section with orthogonal cavity lengths being varied. (a)–(d) Adapted with permission from Ref. [16], © The Optical Society.

relative arrival time of two orthogonal THz components at the exit. This can be seen from Figs. 6(b) and 6(c), which show the temporal locations of the THz waveform peak in horizontal and vertical directions. In this case, the output THz polarization state of the propagation mode along the cavity can be fine-adjusted. As shown in the upper row of Fig. 6(d), transforms from the original linear to elliptical and circular polarization were realized. Furthermore, when stresses along the y axis were applied on the paper cavity of Fig. 6(a), the polarization of the cavity mode would also be varied, as shown in the lower row of Fig. 6(d). By contrast, the chirality has been changed from the left-hand polarization (upper) to the right-hand pattern (lower).

It is worth noting that this method of correlated orthogonal polarization modulation with only one physical impact in one direction could be more efficient than conventional methods to change the optical path of one single polarization component[47]. Furthermore, not only the ambient force, but also the magnetic field, etc., can be used to drive the CARR cavity, thus making related THz devices versatile. For example, we attached a small magnet at the tube port, as shown in Fig. 6(e), which was then positioned in a magnetic field. In this situation, the orthogonal cavity lengths will change synchronously [Figs. 6(f) and 6(g)], achieving a similar purpose of polarization conversion to Fig. 6(d), but in a magneto-optic manner.

4.3. Single-pulse measurements of the THz angular dispersion

In previous applications, only resonant frequencies f_m were studied when the tube inner diameter D was changed, which was based on the relationship shown in Eq. (1). Actually, deduced from Eq. (1), θ_m can also be computed by

$$\theta_m = \arccos\left(\frac{c}{2D} \bigg/ \frac{f_m}{m}\right). \qquad (2)$$

This equation can be utilized to resolve the θ_m ($m = 1, 2, 3$) belonging to the resonant frequency f_m ($m = 1, 2, 3$), as shown in Fig. 7(a). Figure 7(b) further indicates the actual scenario of a Gaussian beam incidence into the CARR cavity and θ varied with the THz frequencies. Therefore, it is possible to retrieve the spatially angular dispersion of a THz beam, i.e., $\theta_m - f_m$, by merely detecting the transmitted THz–CARR spectrum and doing calculations via Eq. (2). It is worth mentioning that θ in Eq. (1) describes an average of the angle values for all frequency components of the incident light. In other words, θ is independent of THz frequencies in Eq. (1), slightly different from the case of Eq. (2).

One output THz spectrum from the system in Fig. 2(b) is shown in Fig. 7(c). It can be seen that there are five resonant frequencies, and the corresponding f_m/m decreased, as shown as the line slopes in Fig. 7(d). Based on Fig. 7(d) and Eq. (2), the calculated $\theta - f$ are shown in Fig. 7(e), which decreased from 87.5 deg to 86.7 deg with the increasing THz frequency. This achievement is consistent with traditional methods such

as scanning THz imaging or knife-edge measurements (not shown).

In similar ways, two additional measurements of the THz divergence angle under different conditions have been carried out in Figs. 7(f)–7(h) and 7(i)–7(k). First, we introduced an extra TPX lens to enhance the THz beam focusing, thereby increasing the divergence angle, which can also be resolved by our CARR method, as shown in Figs. 7(f)–7(h). Second, we conducted experiments on another widely used THz source, namely, femtosecond laser filamentation[48–51], whose THz emission was also detected by our CARR method. The results revealed an increasing trend of the detected θ angle with respect to the frequency [Figs. 7(i)–7(k)], which differs from the PCA experiments [Figs. 7(e) and 7(h)] but aligns with the conclusions in field of THz radiation during laser filamentation given by the well-known off-axis phase-matching model[52]. Briefly, as the two-color laser pulses propagate along the filament, there is an accumulation of their phase difference. Consequently, the generated THz waves at different positions along the filament exhibit different polarities, resulting in an interference pattern in the far field, namely, a ring-shaped distribution. Specifically, the phase matching for longer-wavelength THz components requires a larger divergence angle (i.e., a smaller θ), while that for shorter-wavelength components requires a smaller divergence angle (i.e., a larger θ). This leads to a trend that low THz frequencies are distributed in the outer ring with high frequencies in the inner ring.

So far, this has proved the validity of the CARR cavity on angular dispersion recording on the THz spectrum. All signals that need to be detected are single THz pulses in the time domain and their spectrum can be obtained by the Fourier transform. This CARR method has significantly sped up the measurement processes compared with traditional ways like scanning imaging and knife-edge detection, which need multiple repeat measurements at different longitudinal locations of the THz beam before resolving its angular dispersion information.

5. Brief Introduction to the Numerical Simulation Method of the CARR Effect

In order to examine the experimental CARR effect, numerical simulations can be performed by the commercial software RSoft[15–17]. Our experimental parameters of $D = 8$–16 mm, $t = 0.08$ mm, and $n' = 1.6$, as well as $L = 15$ cm and $\theta = 85$ deg were all taken into consideration while building the numerical model. The software will sequentially simulate the result of single-frequency THz waves passing through the waveguide within the set frequency range and display the real-time THz energy distribution along the tubular structures. After the frequency scanning is completed, the transmission THz spectrum will be output, inside which resonant dips are clearly observed. More importantly, these frequency positions can be well explained by Eq. (1). This numerical simulation approach
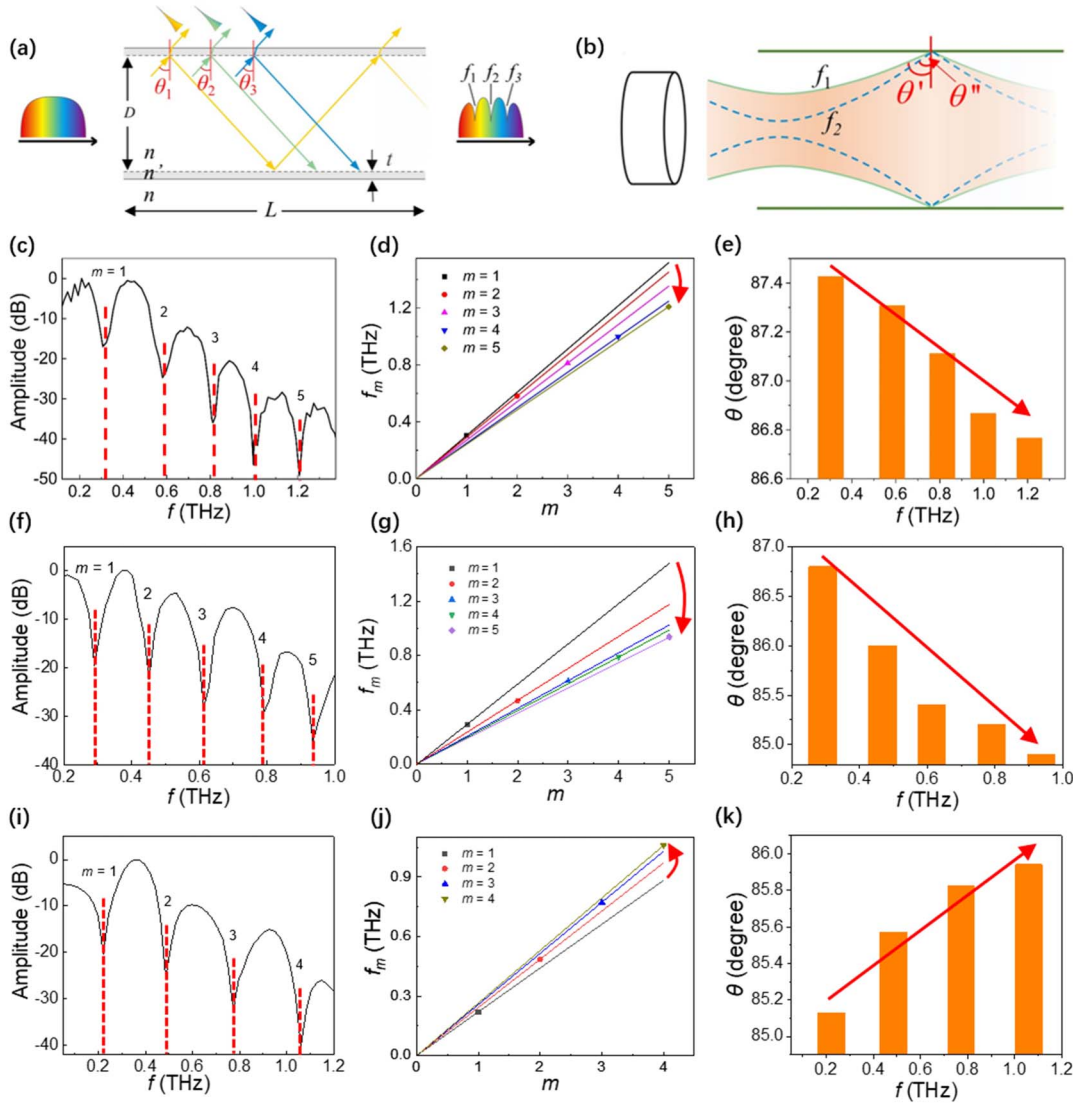
Fig. 7. (a), (b) $\theta_m - f_m$ connection in the CARR principle; (c) THz transmission spectrum of the paper cavity with the THz source in Fig. 2; (d) corresponding resonant frequencies at different orders m retrieved from (c); (e) calculated $\theta - f$ distribution by data in (d) and Eq. (2); (f)–(h) an additional TPX lens was inserted into the THz beam to enhance the THz divergence angle, which was then detected by the CARR method; (i)–(k) THz radiation from a laser plasma filament was detected by the CARR method. (a)–(k) Adapted from Ref. [17] under the license CC BY 4.0.

has been often used in our research on CARR, allowing us to verify the experimental results under ideal conditions.

6. Conclusion and Outlook

In this work, we first reviewed the origins of the CARR mechanism, highlighting its similarities and differences with existing theories such as antiresonance and multimode interference. Then, we emphasized its unique spectral characteristics that are independent of cladding materials and geometries. Finally, we explored diverse applications of CARR, including the pressure sensing using paper-folded tubes, THz polarization modulations driven by force or magnetism, and single-pulse measurements of THz angular dispersion.

Looking ahead, the CARR effect promises to enable more potential advancements in the fields of physics[53,54], biophotonics[55], and material science, as achieved by the typical antiresonance mechanism, and future research could explore its use in novel THz devices and systems, such as sensors, modulators, and filters. Additionally, investigations into the optimization of the CARR structure and the exploration of different tubular materials may further enhance its performance and broaden its practical applications. Currently, some works are still underway, such as the CARR-inspired 360-deg leaky-wave antenna aimed at THz wireless communications, and CARR tube-based applications involving 4D printing materials, soft magnetic materials, and kirigami/origami materials, etc., as the cladding wall. It is also worth mentioning that, although we proved the theory with millimeter-diameter tubes and THz waves, the presented CARR

technique promises to be generalized to tubular structures in other sizes by using light sources with proper wavelengths after carefully considering the scaling law. For example, along a laser plasma filament with a diameter of ∼100 μm, the leaky F–P effect might also exist[56]. Hence, this CARR principle has provided a new degree of freedom towards interactions between light and tubular entities.

Acknowledgement

References

1. C. L. Wei, R. J. Weiblen, C. R. Menyuk, and J. Hu, "Negative curvature fibers," Adv. Opt. Photonics **9**, 504 (2017).
2. W. Ding, Y. Y. Wang, S. F. Gao, M. L. Wang, and P. Wang, "Recent progress in low-loss hollow-core anti-resonant fibers and their applications," IEEE J. Sel. Top. Quantum Electron. **26**, 4400312 (2020).
3. F. Yu and J. C. Knight, "Negative curvature hollow core optical fiber," IEEE J. Sel. Top. Quantum Electron. **22**, 8000106 (2016).
4. W. Ding, Y. Y. Wang, S. F. Gao, Y. F. Hong, and P. Wang, "Theoretical and experimental investigation of light guidance in hollow-core anti-resonant fiber," Acta Phys. Sin. **67**, 124201 (2018).
5. C. H. Lai, Y. C. Hsueh, H. W. Chen, Y. Huang, H. Chang, and C. K. Sun, "Low-index terahertz pipe waveguides," Opt. Lett. **34**, 3457 (2009).
6. F. Davidson-Marquis, J. Gargiulo, E. Gómez-López, B. Jang, T. Kroh, C. Müller, M. Ziegler, S. A. Maier, H. Kübler, M. A. Schmidt, and O. Benson, "Coherent interaction of atoms with a beam of light confined in a light cage," Light Sci. Appl. **10**, 114 (2021).
7. J. Kim, B. Jang, J. Gargiulo, J. Bürger, J. B. Zhao, S. Upendar, T. Weiss, S. A. Maier, and M. A. Schmidt, "The optofluidic light cage–on-chip integrated spectroscopy using an antiresonance hollow core waveguide," Anal. Chem. **93**, 752 (2021).
8. W. G. Yang, D. B. Conkey, B. Wu, D. L. Yin, A. R. Hawkins, and H. Schmidt, "Atomic spectroscopy on a chip," Nat. Photonics **1**, 331 (2007).
9. H. Schmidt and A. R. Hawkins, "Atomic spectroscopy and quantum optics in hollow-core waveguides," Laser Photonics Rev. **4**, 720 (2010).
10. B. Wu, J. F. Hulbert, E. J. Lunt, K. Hurd, A. R. Hawkins, and H. Schmidt, "Slow light on a chip via atomic quantum state control," Nat. Photonics **4**, 776 (2010).
11. M. N. Velasco-Garcia, "Optical biosensors for probing at the cellular level: a review of recent progress and future prospects," Semin. Cell Dev. Biol. **20**, 27 (2009).
12. V. M. N. Passaro, F. Dell'Olio, B. Casamassima, and F. D. Leonardis, "Guided-wave optical biosensors," Sensors **7**, 508 (2007).
13. W. J. Ni, C. Y. Yang, Y. Y. Luo, R. Xia, P. Lu, D. J. J. Hu, S. Danto, P. P. Shum, and L. Wei, "Recent advancement of anti-resonant hollow-core fibers for sensing applications," Photonics **8**, 128 (2021).
14. K. Benaissa and A. Nathan, "Silicon anti-resonant reflecting optical waveguides for sensor applications," Sens. Actuators A Phys. **65**, 33 (1998).
15. J. Y. Zhao, J. A. Yan, Z. H. Dong, C. Liu, Y. P. Han, Y. Peng, W. Lin, and Y. M. Zhu, "Cladding-free antiresonance in tubular structures," Adv. Photonics Res. **3**, 2200148 (2022).
16. J. Y. Zhao, J. A. Yan, Y. P. Han, L. Lao, Y. Peng, and Y. M. Zhu, "Paper-folding-based terahertz anti-resonant cavity," Opt. Lett. **48**, 704 (2023).
17. Y. Han, J. Zhao, Q. Wang, J. Yan, Y. Yao, J. Xiao, C. Liu, F. Zhu, L. Lao, and Y. Peng, "Recording the angular dispersion of a terahertz beam into its frequency spectrum for fast measurements," Opt. Express **31**, 28999 (2023).
18. J. C. Fan and N. A. Kotov, "Chiral nanoceramics," Adv. Mater. **32**, 1906738 (2020).
19. W. M. Li, G. S. Huang, J. Wang, Y. Yu, X. J. Wu, X. G. Cui, and Y. F. Mei, "Superelastic metal microsprings as fluidic sensors and actuators," Lab Chip **12**, 2322 (2012).
20. Y. Q. Wang, Y. Wang, G. S. Huang, Y. Kong, C. Liu, Z. Zhao, K. B. Wu, and Y. F. Mei, "Single whispering gallery mode in mesh-structured tubular microcavity with tunable axial confinement," Adv. Photonics Res. **2**, 2000163 (2021).
21. R. Briche, A. Benamrouche, P. Cremillieu, P. Regreny, J. L. Leclercq, X. Letartre, A. Danescu, and S. Callard, "Tubular optical microcavities based on rolled-up photonic crystals," APL Photonics **5**, 106106 (2020).
22. A. Danescu, P. Regreny, P. Cremillieu, and J. L. Leclercq, "Fabrication of self-rolling geodesic objects and photonic crystal tubes," Nanotechnology **29**, 285301 (2018).
23. Z. A. Tian, L. N. Zhang, Y. F. Fang, B. R. Xu, S. W. Tang, N. Hu, Z. H. An, Z. Chen, and Y. F. Mei, "Deterministic self-rolling of ultrathin nanocrystalline diamond nanomembranes for 3D tubular/helical architecture," Adv. Mater. **29**, 1604572 (2017).
24. Z. Y. Zhang, Z. A. Tian, Y. F. Mei, and Z. F. Di, "Shaping and structuring 2D materials via kirigami and origami," Mater. Sci. Eng. R Rep. **145**, 100621 (2021).
25. L. A. Hof and J. A. Ziki, "Micro-hole drilling on glass substrates—a review," Micromachines **8**, 53 (2017).
26. C. Themistos, K. Kalli, M. Komodromos, C. Markides, A. Quadir, B. M. A. Rahman, and K. T. V. Grattan, "Low-loss multimode interference couplers for terahertz waves," Proc. SPIE **8426**, 84260X (2012).
27. J. Canning and A. L. G. Carter, "Modal interferometer for in situ measurements of induced core index change in optical fibers," Opt. Lett. **22**, 561 (1997).
28. G. Z. Liu, C. Chang, Z. Qiao, K. J. Wu, Z. Zhu, G. Q. Cui, W. Y. Peng, Y. Z. Tang, J. Li, and C. H. Fan, "Myelin sheath as a dielectric waveguide for signal propagation in the mid-infrared to terahertz spectral range," Adv. Funct. Mater. **29**, 1807862 (2019).
29. H. Wang, H. L. Zhen, S. L. Li, Y. L. Jing, G. S. Huang, Y. F. Mei, and W. Lu, "Self-rolling and light-trapping in flexible quantum well-embedded nanomembranes for wide-angle infrared photodetectors," Sci. Adv. **2**, e1600027 (2016).
30. H. D. Bai, S. Li, J. Barreiros, Y. Q. Tu, C. R. Pollock, and R. F. Shepherd, "Stretchable distributed fiber-optic sensors," Science **370**, 848 (2020).
31. L. Stern, B. Desiatov, I. Goykhman, and I. Levy, "Nanoscale light–matter interactions in atomic cladding waveguides," Nat. Commun. **4**, 1548 (2013).
32. K. A. Baksheeva, R. V. Ozhegov, G. N. Goltsman, N. V. Kinev, V. P. Koshelets, A. Kochnev, N. Betzalel, A. Puzenko, P. B. Ishai, and Y. Feldman, "The sub THz emission of the human body under physiological stress," IEEE Trans. Terahertz Sci. Technol. **11**, 381 (2021).
33. D. W. Vogt, J. Anthony, and R. Leonhardt, "Metallic and 3D-printed dielectric helical terahertz waveguides," Opt. Express **23**, 33359 (2015).
34. P. X. Gao, Y. Ding, W. J. Mai, W. L. Hughes, C. S. Lao, and Z. L. Wang, "Conversion of zinc oxide nanobelts into superlattice-structured nanohelices," Science **309**, 1700 (2005).
35. Y. Qin, Y. Kim, L. B. Zhang, S. Lee, R. B. Yang, A. L. Pan, K. Mathwig, M. Alexe, U. Gösele, and M. Knez, "Preparation and elastic properties of helical nanotubes obtained by atomic layer deposition with carbon nanocoils as templates," Small **6**, 910 (2010).
36. Y. Q. Zhou and M. Karplus, "Interpreting the folding kinetics of helical proteins," Nature **401**, 400 (1999).
37. S. O. Kelley and J. K. Barton, "Electron transfer between bases in double helical DNA," Science **283**, 375 (1999).
38. A. J. Wang, G. J. Quigley, F. J. Kolpak, G. van der Marel, J. H. van Boom, and A. Rich, "Left-handed double helical DNA: variations in the backbone conformation," Science **211**, 171 (1981).
39. Y. Guo, M. Zhong, Z. Fang, P. Wan, and G. Yu, "A wearable transient pressure sensor made with MXene nanosheets for sensitive broad-range human-machine interfacing," Nano Lett. **19**, 1143 (2019).
40. Y. Lu, X. Qu, W. Zhao, Y. Ren, W. Si, W. Wang, Q. Wang, W. Huang, and X. Dong, "Highly stretchable, elastic, and sensitive MXene-based hydrogel for flexible strain and pressure sensors," Research **2020**, 2038560 (2020).

41. G. Ge, Y. Zhang, J. Shao, W. Wang, W. Si, W. Huang, and X. Dong, "Stretchable, transparent, and self-patterned hydrogel-based pressure sensor for human motions detection," Adv. Funct. Mater. **28**, 1802576 (2018).

42. Z. Wang, Y. Si, C. Zhao, D. Yu, W. Wang, and G. Sun, "Flexible and washable poly (ionic liquid) nanofibrous membrane with moisture proof pressure sensing for real-life wearable electronics," ACS Appl. Mater. Interfaces **11**, 27200 (2019).

43. X. Wu, Z. Li, H. Wang, J. Huang, J. Wang, and S. Yang, "Stretchable and self-healable electrical sensors with fingertip-like perception capability for surface texture discerning and biosignal monitoring," J. Mater. Chem. C **7**, 9008 (2019).

44. M. Xu, F. Li, Z. Zhang, T. Shen, and J. Qi, "Piezoresistive sensors based on rGO 3D microarchitecture: coupled properties tuning in local/integral deformation," Adv. Electron. Mater. **5**, 1800461 (2018).

45. M. Jian, K. Xia, Q. Wang, Z. Yin, H. Wang, C. Wang, H. Xie, M. Zhang, and Y. Zhang, "Flexible and highly sensitive pressure sensors based on bionic hierarchical structures," Adv. Funct. Mater. **27**, 1606066 (2017).

46. G. Ge, W. Yuan, W. Zhao, Y. Lu, Y. Zhang, W. Wang, P. Chen, W. Huang, W. Si, and X. Dong, "Highly stretchable and autonomously healable epidermal sensor based on multi-functional hydrogel frameworks," J. Mater. Chem. A **7**, 5949 (2019).

47. X. Luo, Z. Tan, W. Wang, C. Wang, and J. Cao, "An efficient terahertz polarization converter with highly flexible tunability over an ultra-broad bandwidth," J. Appl. Phys. **125**, 144901 (2019).

48. J. Zhao, W. Chu, Z. Wang, Y. Peng, C. Gong, L. Lin, Y. Zhu, W. Liu, Y. Cheng, S. Zhuang, and Z. Xu, "Strong spatial confinement of terahertz wave inside femtosecond laser filament," ACS Photonics **3**, 2338 (2016).

49. J. Zhao, W. Chu, L. Guo, Z. Wang, J. Yang, W. Liu, Y. Cheng, and Z. Xu, "Terahertz imaging with sub-wavelength resolution by femtosecond laser filament in air," Sci. Rep. **4**, 3880 (2014).

50. J. Zhao, W. Liu, S. Li, D. Lu, Y. Zhang, Y. Peng, Y. Zhu, and S. Zhuang, "Clue to a thorough understanding of terahertz pulse generation by femtosecond laser filamentation," Photonics Res. **6**, 296 (2018).

51. J. Zhao, Q. Wang, Y. Hui, Y. Chen, F. Zhu, Z. Jin, A. P. Shkurinov, Y. Peng, Y. Zhu, S. Zhuang, and L. Lao, "Traveling-wave antenna model for terahertz radiation from laser-plasma interactions," SciPost Phys. Core **5**, 046 (2022).

52. Y. S. You, T. I. Oh, and K. Y. Kim, "Off-axis phase-matched terahertz emission from two-color laser-induced plasma filaments," Phys. Rev. Lett. **109**, 183902 (2012).

53. Y. Zhu, X. Zang, H. Chi, Y. Zhou, Y. Zhu, and S. Zhuang, "Metasurfaces designed by a bidirectional deep neural network and iterative algorithm for generating quantitative field distributions," Light Adv. Manuf. **4**, 9 (2023).

54. X. Zang, B. Yao, L. Chen, J. Xie, X. Guo, A. V. Balakin, A. P. Shkurinov, and S. Zhuang, "Metasurfaces for manipulating terahertz waves," Light Adv. Manuf. **2**, 10 (2021).

55. Y. Peng, J. Huang, J. Luo, Z. Yang, L. Wang, X. Wu, X. Zang, C. Yu, M. Gu, Q. Hu, X. Zhang, Y. Zhu, and S. Zhuang, "Three-step one-way model in terahertz biomedical detection," PhotoniX **2**, 12 (2021).

56. C. Liu, Y. Chen, J. Zhao, L. Tang, Y. Peng, and Y. Zhu, "Plasma micro-cavity of terahertz wave during laser filamentation," IEEE Photon. J. **11**, 5900714 (2019).